Structure and Optical Properties of the Li2In2GeSe6 Crystal

A. P. Yelisseyev,*[†,‡] M. S. Molokeev,[§,∥,⊥] Xingxing Jiang,[#] P. G. Krinitsin,[†] L. I. Isaenko,[†,‡] and Zheshuai Lin*[#,¶]

[†]Sobolev Institute of Geology and Mineralogy RAS, 3 Ac. Koptyug Avenue, Novosibirsk 630090, Russia
[‡]Novosibirsk State University, 2 Pyrogova Street, 630090 Novosibirsk, Russia
[§]Laboratory of Crystal Physics, Kirensky Institute of Physics, Federal Research Center KSC SB RAS, Krasnoyarsk 660036, Russia
[∥]Department of Physics, Far Eastern State Transport University, Khabarovsk 680021, Russia
[⊥]Siberian Federal University, Krasnoyarsk 660041, Russia
[#]Technical Institute of Physics and Chemistry, Chinese Academy of Sciences, Beijing 100190, PR China
[¶]University of Chinese Academy of Sciences, Beijing 100190, PR China

S *Supporting Information*

ABSTRACT: Intense search for new nonlinear optical crystals for the mid-infrared region is in progress, and Li-containing quaternary chalcogenides are expected to improve transparency range, stability, phase-matching conditions, and other parameters in comparison with commercially available $AgGaS_2$, $AgGaSe_2$, and $ZnGeP_2$. Single crystals of $Li_2In_2GeSe_6$ up to 8 mm in size were obtained by the Bridgman−Stockbarger growth technique, and their high quality was confirmed by exciton luminescence. A monoclinic structure and direct band-to-band electronic transitions were established, and the thermal expansion was shown to be virtually isotropic. Defect-related absorption and luminescence were revealed, and the way to lower them was suggested. The electronic structure, density of states, and some optical properties were calculated from the first principles for $Li_2In_2GeSe_6$. The calculated nonlinear coefficients and rather large birefringence indicate a strong phase-matching ability. These investigations demonstrate that $Li_2In_2GeSe_6$ is a promising mid-infrared nonlinear optical crystal.
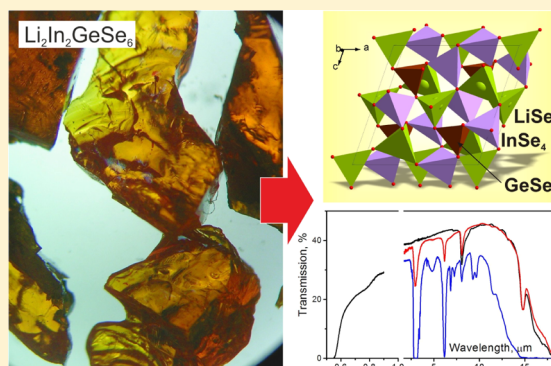
1. INTRODUCTION

Frequency conversion using nonlinear optical (NLO) crystals is an effective way to generate coherent radiation in the mid- and far-infrared (IR) regions. Such laser sources have many important civil and military applications including atmospheric monitoring, laser radar, and laser guidance. Since the 1970s, the most widely used NLO crystals are the chalcopyrite-type $AgGaC_2$ (C = S and Se) and $ZnGeP_2$ crystals.[1] Although these crystals have large NLO coefficients and a wide transparent range in the IR range, they also possess serious disadvantages in their properties. For example, all of these chalcopyrite-type crystals are strongly anisotropic in their thermal expansion coefficients, $AgGaC_2$ (C = S and Se) has a low laser damage threshold, $AgGaSe_2$ is not phase-matchable at 1 μm, and $ZnGeP_2$ exhibits strong two-photon absorption of the conventional 1 μm (Nd:YAG) or 1.55 μm (Yb:YAG) laser-pumping sources.[2] Thus, the search for new IR NLO materials with better overall properties is in progress.

Two ways can be used to overcome these drawbacks. One way is to replace Ag with Li and to grow crystals of the $LiBC_2$ family, where B = In and Ga and C = S, Se, and Te with an orthorhombic structure (except tellurides). These crystals have significantly higher thermal conductivity, nearly isotropic thermal expansion, and a large band gap up to 4 eV. As a result, the optical damage thresholds of $LiBC_2$ crystals exceed those of their Ag-containing analogues, although the nonlinear susceptibility of Li compounds is slightly lower.[3−5] The other way is to synthesize quaternary compounds. For example, crystal $AgGaGeS_4$, which is a solid solution of $AgGaS_2$ and GeS_2, demonstrates improved laser damage thresholds and an extended range of phase-matching tuning in comparison with its parent compounds.[6−8] In the last few years, there were attempts to combine these two approaches and to create a quaternary compound based on both $LiGaS_2$ and GeS_2: fine-grained powder of $Li_2Ga_2GeS_6$ was synthesized.[9] The next step was $LiGaGe_2Se_6$.[10] Both of these compounds crystallize in an orthorhombic structure. Single crystals of $LiGaGe_2Se_6$ were grown and studied in detail.[11,12] The advantages of $LiGaGe_2Se_6$ are higher nonlinear susceptibility (d_{15} = 18.6 pm/V and d_{33} = 12.8 pm/V[10]) and lower melting temperature

(710 °C): the corresponding parameters for LiGaSe$_2$ are d_{31} = 10 pm/V[13] and 915 °C.[10,13] A decrease in the melting temperature lowers the risk of incongruent evaporation when crystal is being grown. A probable consequence of such evaporation is a deviation from the stoichiometric composition and appearance of inclusions of side phases. The latter results in an increase in the light scattering and a decrease in the optical damage threshold.

In the quaternary Li−Ga−Ge−Se compounds, the microscopic NLO-active unit is the (Ga/Ge)Se$_4$ tetrahedron. Considering that the heavier group III element, In, will increase the NLO response and birefringence owing to the larger polarization of the electrons, Li$_2$In$_2$GeSe$_6$ powder was synthesized.[14] The preliminary experiments revealed that this compound is crystallized in the noncentrosymmetric monoclinic space group Cc with a three-dimensional framework composed of corner-sharing LiSe$_4$, InSe$_4$, and GeSe$_4$ tetrahedra. The band gap was estimated to be 2.30 eV from the reflection spectra, and the second harmonic generation (SHG) signal at 2.090 μm pumping was found to be close to that of AgGaSe$_2$.[14] Besides, this Li-containing selenide may be a promising crystal for neutron detection.[15,16] As for the potential application, crystal growth habit, optical transmittance, and thermal expansion are also crucial factors directly influencing the performance, which, however, have not been studied.

To shed light on the application prospect of Li$_2$In$_2$GeSe$_6$, in the present work, we grew large single crystals of Li$_2$In$_2$GeSe$_6$ and redetermined its structure. The quality of the grown crystal was evaluated by luminescence spectrum, and its optical transmittance and thermal expansion behavior were studied. Meanwhile, in combination with Raman spectrum, first-principles calculation on the electronic structure, lattice vibration property, and optical property was also performed to clarify the structure−property relationship.

2. EXPERIMENTAL SECTION

2.1. Synthesis and Growth of the Li$_2$In$_2$GeSe$_6$ Crystal.
When growing Li-containing compounds from elementary starting reagents, it is necessary to take into account the high chemical activity of metallic lithium and the high pressure of selenium vapor. Because of these features, melting of components can lead to the destruction of the crucible. Moreover, the uniformity and stoichiometry of the synthesized charge are considerably violated, which will necessarily lower crystal quality.

Weighing and loading of elementary starting reagents were carried out in a dry camera flushed by pure argon. Little deviations from stoichiometry during synthesis resulting from high Li activity and GeSe$_2$ volatility were corrected by adding a surplus of some components. After loading the starting reagents into a glassy carbon crucible, the latter was placed inside a quartz ampule. Glassy carbon is the only available material that is resistant to Li and its melted compounds at temperatures up to 1000 °C. The glassy carbon crucible excludes direct contact between reagents and quartz. The quartz ampule was evacuated, filled with Ar, and sealed off.

To synthesize Li$_2$In$_2$GeSe$_6$, the quartz ampule with the glassy carbon crucible inside was located into a tubular resistance furnace. Heating of the furnace up to the completion of synthesis reaction was carried out in two stages. The first stage was a rather slow heating to 300 °C at a rate of 5°/h, and the second one was a fast heating to 800 °C at a rate of 20°/h.

Then, the ampule was kept at 800 °C for a day and cooled to room temperature in a regime of switched off furnace.

We obtained tight fine-grained dark red ingots with a content of the Li$_2$In$_2$GeSe$_6$ phase close to 100% according to X-ray diffraction (XRD) data. Splitting and loading of the ingots were carried out in an Ar atmosphere. The ampule with the charge was evacuated and sealed off. To grow Li$_2$In$_2$GeSe$_6$ single crystals, we used the Bridgman−Stockbarger technique. The growth ampule was located in a vertical resistance furnace. The furnace of special design provides a high temperature gradient of about 40 °C/cm on the crystallization front at minimum overheating of the liquid phase: this is particularly important when growing single crystals of multicomponent compounds. This allowed us to minimize the stoichiometry violation and provided the most favorable conditions on the crystallization front. The growth rate was about 2 mm/day in all of these experiments. After the crystal growth process, the furnace was cooled at a rate of about 10 °C/h.

2.2. X-ray Diffraction.
The powder diffraction data of Li$_2$In$_2$GeSe$_6$ for Rietveld analysis were collected at room temperature with a Bruker D8 ADVANCE powder diffractometer (Cu Kα radiation) and a linear VANTEC detector. The average grain size in the Li$_2$In$_2$GeSe$_6$ powder used for the XRD experiments was 35 nm. The step size of 2θ was 0.016°, and the counting time was 1.5 s per step. A 2θ range of 9−70° was measured with a 0.6 mm divergence slit, but a 2θ range of 70−140° was measured with a 2 mm divergence slit. Larger slits allow a noticeable increase in the intensity of high-angle peaks without loss of resolution because the high-angle peaks are broad enough not to be affected by a bigger divergence beam. The estimated standard deviations (esd's) $\sigma(I_i)$ of all points on patterns were calculated using intensities I_i: $\sigma(I_i)$ = $I_i^{1/2}$. The intensities and obtained esd's were further normalized: $I_{i\,norm}$ = I_i × 0.6/(slit width) and $\sigma_{norm}(I_i)$ = $\sigma(I_i)$ × 0.6/(slit width), taking into account the actual value of the divergence slit width, which was used to measure each particular intensity I_i, and saved in a xye-type file. Therefore, the transformed powder pattern has a typical view in the whole 2θ range 9−140°, but all high-angle points have small esd's.

2.3. Optical Properties.
Transmission spectra were recorded using a UV-2501 PC Shimadzu spectrometer in the UV to near-IR region, whereas in the mid-IR region, we used a Fourier transform spectrometer Infralum 801. We analyzed the shape of the shortwave absorption edge and constructed Tauc plots[17] to establish the type of the band-to-band electronic transitions for thin plates of Li$_2$In$_2$GeSe$_6$. Band gap values were calculated for different temperatures in the 80−350 K range. Raman spectra were measured at 300 K using a HORIBA Jobin Yvon LabRAM HR800 spectrometer with a 1024 pixel LN/CCD detector at 532 nm excitation. The same spectrometer was used to record photoluminescence (PL) spectra at 325 and 532 nm excitations from Cd−He and solid-state diode-pumped Nd:YAG (second harmonic) lasers, respectively.

2.4. First-Principles Calculations.
The first-principles calculations are performed by the plane-wave pseudopotential density functional theory (DFT)[18,19] implemented by the CASTEP package.[20] The generalized gradient approximation (GGA) with a Perdew−Burke−Ernzerhof (PBE) functional[21] is adopted, and the ion−electron interactions are modeled by the optimized normal-conserving pseudopotentials[22] for all elements. A kinetic energy cutoff of 800 eV and Monkhorst−Pack[23] k-point meshes with a spanning grid less than 0.04/Å^3 in the Brillouin zone are chosen.

Because of the discontinuity of exchange–correlation, the GGA-predicted band gaps are always smaller than the experimental values, and scissors operator[24] was used to raise the conduction bands (CBs) to match the calculated band gap with the measured value. On the basis of the scissors-corrected electron structures, the SHG coefficients were calculated by the formula developed by Lin et al. based on the gauge formalism method:[25,26]

$$\chi^{ijk} = \chi^{ijk}(\text{VE}) + \chi^{ijk}(\text{VH}) + \chi^{ijk}(\text{two bands})$$

where $\chi^{ijk}(\text{VE})$ and $\chi^{ijk}(\text{VH})$ denote the contributions from virtual-electron processes and virtual-hole processes, respectively, and $\chi^{ijk}(\text{two bands})$ gives the contribution from two band processes to $\chi^{(2)}$. The formulas for calculating $\chi^{ijk}(\text{VE})$, $\chi^{ijk}(\text{VH})$, and $\chi^{ijk}(\text{two bands})$ are as follows

$$\chi^{ijk}(\text{VE}) = \frac{e^3}{2\hbar^2 m^3} \sum_{vcc'} \int \frac{d^3\vec{k}}{4\pi^3} P(ijk) \text{Im}[p_{vc}^i p_{cc'}^j p_{c'v}^k]$$
$$\left(\frac{1}{\omega_{cv}^3 \omega_{vc'}^2} + \frac{2}{\omega_{vc}^4 \omega_{c'v}} \right)$$

$$\chi^{ijk}(\text{VH}) = \frac{e^3}{2\hbar^2 m^3} \sum_{vv'c} \int \frac{d^3\vec{k}}{4\pi^3} P(ijk) \text{Im}[p_{vv'}^i p_{v'c}^j p_{cv}^k]$$
$$\left(\frac{1}{\omega_{cv}^3 \omega_{v'c}^2} + \frac{2}{\omega_{vc}^4 \omega_{cv'}} \right)$$

$$\chi^{ijk}(\text{two bands}) = \frac{e^3}{\hbar^2 m^3}$$
$$\sum_{vc} \int \frac{d^3\vec{k}}{4\pi^3} P(ijk)$$
$$\frac{\text{Im}[p_{vc}^i p_{cv}^j (p_{vv}^k - p_{cc}^k)]}{\omega_{vc}^5}$$

Here, i, j, and k are Cartesian components, v and v' denote valence band (VB), and c and c' denote CB. $P(ijk)$ denotes full permutation. The absorption, that is, the imaginary part of the dielectric function, can be calculated by the electronic transition across the forbidden band. Therefore, using the Kramers–Kronig transformation, the refractive index, that is, the real part, can be determined.[27] The vibrational properties were calculated by linear response formalism,[28] in which the phonon frequencies were obtained by the second derivative of the total energy with respect to a given perturbation.[29]

3. RESULTS AND DISCUSSION

3.1. Crystal Structure. A $Li_2In_2GeSe_6$ boule is shown in Figure 1. The typical boule (Figure 1a) was 20 mm in diameter and ~20 mm in length. Several transparent single crystal pieces with a color varying from yellow to brown, up to 6 mm in size, are given in the (b) section. Study of $Li_2In_2GeSe_6$ pieces shown in Figure 1b in polarized light under a microscope showed that they are all single crystals.

The reasons for the variation of color in Figure 1b are the complicated shape of the $Li_2In_2GeSe_6$ pieces and different thicknesses of the samples. The color may be red for thick plates (the same in the bulk of the boule in Figure 1a). Green
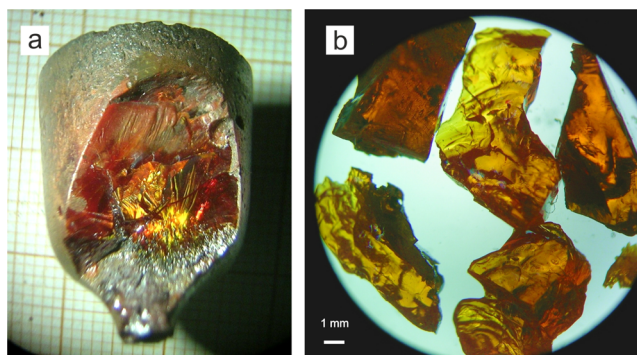

Figure 1. Boule of $Li_2In_2GeSe_6$ (a) and several single crystal pieces (b).

color in some parts of the boule may be due to some side phases on its boundary.

Rietveld refinement was performed by using TOPAS 4.2,[30] which accounts esd's of each point by a special weight scheme. All peaks were indexed by a monoclinic cell (Cc) with parameters close to those of $Li_2In_2GeSe_6$,[14] and refinement was stable and gave low R-factors (Table 1 and Figure 2a). The x

Table 1. Main Parameters of Processing and Refinement of the Li₂In₂GeSe₆ Sample

compound	$Li_2In_2GeSe_6$
space group	Cc
a, Å	12.7296(6)
b, Å	7.4553(4)
c, Å	12.6798(8)
β, deg	109.839(3)
V, Å³	1131.9(1)
Z	4
2θ-interval, deg	9−140
R_{wp}, %	3.97
R_p, %	3.29
R_{exp}, %	2.84
χ^2	1.40
R_B, %	1.25

and z coordinates of Li1 ion were fixed because the Cc space group (m point group) has origin in the c plane and this requires fixing x and z coordinates of one ion. The coordinates of atoms and main bond lengths are in Tables S1 and S2, respectively. The crystal structure of $Li_2In_2GeSe_6$ is presented in Figure 2b. $Li_2In_2GeSe_6$ crystallizes in the noncentrosymmetric space group Cc of the monoclinic system. In the asymmetric unit, there are two crystallographically independent Li atoms, two independent In atoms, one Ge atom, and six Se atoms. All of the atoms are in general positions with 100% occupancy, and there is no detectable disorder among Li, In, or Ge atoms in the structure, although the possibility of such disorder cannot be completely ruled out. As there are no Se−Se bonds in the structures, the oxidation states of 1+, 3+, 4+, and 2− can be assigned to Li, In, Ge, and Se, respectively. The $LiSe_4$, $InSe_4$, and $GeSe_4$ tetrahedra are connected to each other via corner-sharing to generate a three-dimensional framework. In comparison, another relative quaternary compound $LiGaGe_2Se_6$ has some differences in the structure. $LiGaGe_2Se_6$ crystallizes in the orthorhombic space group $Fdd2$ with an asymmetric unit containing one crystallographically independ-

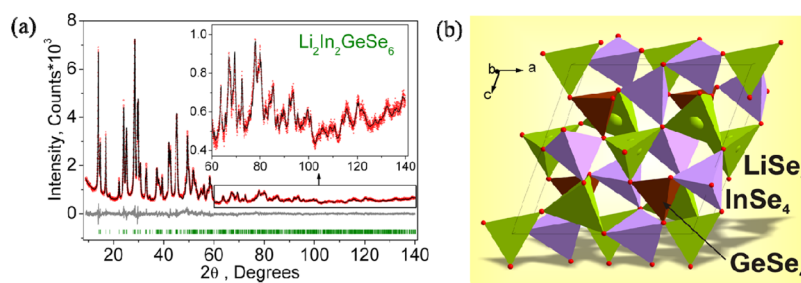**Figure 2.** (a) Rietveld difference plot of $Li_2In_2GeSe_6$ and (b) crystal structure of $Li_2In_2GeSe_6$.

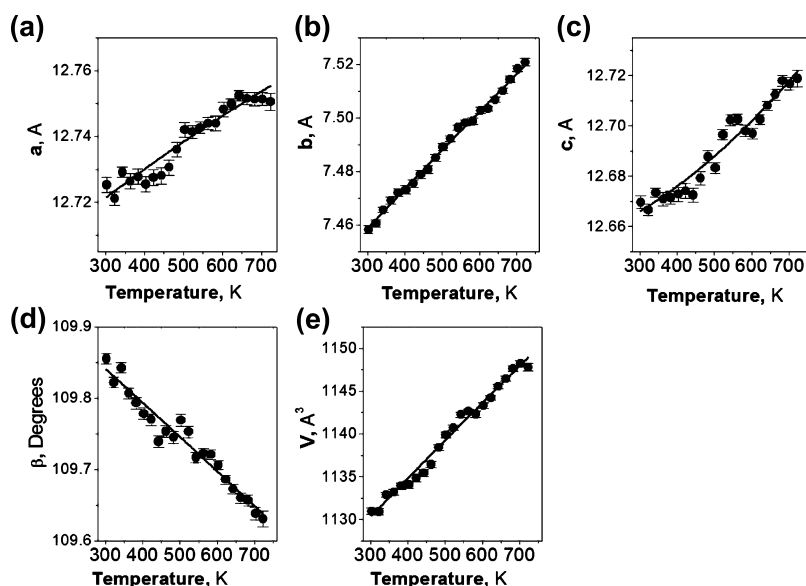**Figure 3.** Thermal dependences of cell parameters a (a), b (b), c (c), β (d), and cell volume V (e) of $Li_2In_2GeSe_6$.

ent Li atom at the Wyckoff position 16b with 50% occupancy, one independent Ga atom at the Wyckoff position 8a, one independent Ge atom at the Wyckoff position 16b, and three independent Se atoms at the Wyckoff position 16b, leading to a $LiGaGe_2Se_6$ stoichiometry.[12,14] $LiGaGe_2Se_6$ also has a three-dimensional framework built up from corner-sharing $LiSe_4$, $GaSe_4$, and $GeSe_4$ tetrahedra, but the Li position is only half-occupied in $LiGaGe_2Se_6$.

Selected bond distances are listed in Table S2. As for the two selenides, the Li−Se distances of 2.62(6)−2.82(8) Å are in good agreement with those of 2.64(3)−2.83(3) Å in $LiGaGe_2Se_6$;[10] the In−Se distances range from 2.52(7) to 2.64(12) Å, which resemble those of 2.569 Å in $LiInSe_2$;[31] and the Ge−Se distances range from 2.28(6) to 2.34(9) Å, which are in good agreement with those in $Ag_2In_2GeSe_6$ (2.313−2.336 Å).

To get information on the temperature dependence of the unit cell parameters (Figure 3), 22 X-ray patterns in the range 2θ from 5° to 120° were collected from 303 to 723 K spending 35 min on each pattern (Figure S1). One can see that all a, b, and c cell parameters and cell volume increase under heating, and therefore the compound has no negative thermal expansion behavior. This differs considerably from the chalcopyrite-like structure (the cases of $AgGaS_2$ and $AgGaSe_2$), where the thermal expansion parameters along and perpendicular to the optical axis are of opposite sign (Table 2). In this table, the average linear thermal expansion coefficients $\alpha_L = (1/L)dL/dT$ for $AgGaSe_2$, $LiInSe_2$, and $Li_2In_2GeSe_6$ are given.

Table 2. Average Linear Thermal Expansion Coefficients $\alpha_L = (1/L)dL/dT$ for $AgGaSe_2$, $LiInSe_2$, and $Li_2In_2GeSe_6$ in the 300−700 K Range (along Different Directions, a, b, and c)

NN	crystal	$\alpha_L \| a$, $\times 10^{-6}$ K^{-1}	$\alpha_L \| b$, $\times 10^{-6}$ K^{-1}	$\alpha_L \| c$, $\times 10^{-6}$ K^{-1}	references
1	$AgGaSe_2$	+28	+28	−16	32
2	$LiInSe_2$	11.5	20.4	8.9	33
3	$Li_2In_2GeSe_6$	6.8	20	12	this paper

One can see that the α_L values for $LiInSe_2$ and $Li_2In_2GeSe_6$ are rather close. The pretty small anisotropy of thermal expansion in $Li_2In_2GeSe_6$ is favorable for the crystal growth.

3.2. Transmission/Absorption Spectra. Transmission spectra for $Li_2In_2GeSe_6$ recorded for 1 and 3 mm thick plates at 300 K are given in Figure 4. The transparency range is 0.55−18 μm for an ∼1 mm thick plate (curves 1−2) and 0.55−15 μm for a 3 mm thick plate (curve 3). The main features in the transparency range are several absorption bands in the mid-IR range, which are listed in Table 3. $Li_2In_2GeSe_6$ crystals of maximal transparency demonstrate two bands near 8.06 and 14.8 μm in their transmission spectra. Following Kokorina's Chalcogenide Glasses book,[34] these bands are associated with Ge−O and Se−Se vibrations. The spectra of other $Li_2In_2GeSe_6$ crystals contain well-pronounced bands near 2.98 and 6.17 μm associated with H_2O and OH$^-$ vibrations: these are stretching and bending vibrations, respectively (curve 2 in Figure 4; Table 3). Keeping the $Li_2In_2GeSe_6$ sample in air results in a considerable increase in water/OH$^-$ absorption: the spectrum

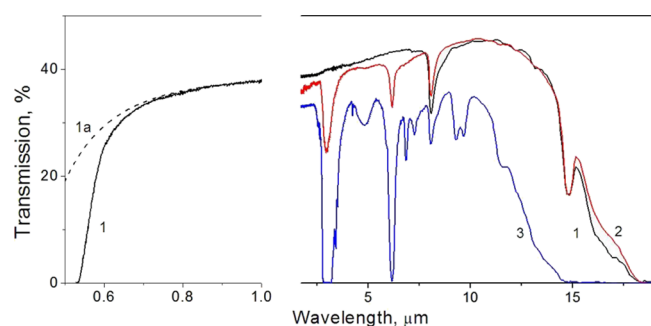**Figure 4.** Transmission spectra for $Li_2In_2GeSe_6$: for 1 mm thick (1, 2) and 3 mm thick (3) samples. T = 300 K. Curve 1a shows the transmission spectrum for a material transparent in the visible range: this spectrum was simulated taking into account Rayleigh light scattering.

Table 3. Interpretation of Absorption in the Mid-IR Region Following Kokorina's Chalcogenide Glasses:[34] Intrinsic and Extrinsic Absorption Bands

NN	wavenumber (cm^{-1})	wavelength (μm)	interpretation	assignment
1	3355	2.98	H_2O	symmetric and asymmetric stretch modes (ν_1 and ν_3)
2	2092	4.78	Se—H	
3	1620	6.17	H_2O	bending vibration, ν_2
4	1464	6.83	?	
5	1375	7.27	Se—H	
6	1240	8.06	Ge—O	
7	1077	9.28	?	
8	1033	9.68	?	
9	675	14.8	H_2O, Se—Se	L_2 libration of H_2O

is shown in Figure 4 (curve 3). There are also other bands near 4.78, 6.84, 7.27, 9.29, and 9.65 μm, and two of these lines (4.78 and 7.27 μm) are associated with Se—H vibrations.[34] The experiments showed that the absorption in the mid-IR region associated with H_2O/OH^- and Se—H vibrations can be restored if the sample is repolished or annealed at a temperature about 300 °C for 2 h. Thus, it is necessary to protect the element surface by a coating in order to keep the transparency. This situation is typical of selenides, whereas the surface of their S-containing analogues is considerably more chemically stable.

One can see a rather low transmission of $Li_2In_2GeSe_6$ samples, which does not exceed 45% even in the mid-IR region. The reason is crystal polishing: we recorded spectra on the cleaved plates of $Li_2In_2GeSe_6$. Until now, we have not been able to find a way to polish this material because of the tendency to delaminate and high chemical activity of the solvents used for polishing. On the other hand, transmission in the envelope of the transmission spectrum monotonically increases as the wavelength grows in the 0.6−12 μm range: this is likely caused by the Rayleigh light scattering on inclusions in $Li_2In_2GeSe_6$.

To determine the type of electronic transitions responsible for the fundamental absorption edge, we prepared a thin plate of $Li_2In_2GeSe_6$, about 60 μm thick. We constructed Tauc plots.[17] Analysis of the shape of the fundamental absorption edge showed that linear approximation is possible for the $(\alpha h\nu)^2$ versus $h\nu$ curves at both 300 and 80 K (Figure 5a). This implies the case of directly allowed band-to-band electronic transitions.[17] Extrapolation of linear part to $\alpha(h\nu)$ = 0 gives the E_g values of 2.27 and 2.46 eV at 300 and 80 K, respectively. As temperature increases from 80 to 300 K, the band gap E_g shifts by 0.19 eV to lower energies: such a shift is rather typical of wide-gap dielectrics.[35]

For a thin plate cut from $Li_2In_2GeSe_6$, we recorded transmission/absorption spectra at 16 different temperatures in the 80−300 K range. For each temperature, the E_g value was estimated. The band gap temperature dependence is given in Figure 5b. The energies were fit with the Varshni equation,[36,37] which is a common empirical fitting for the temperature dependence of semiconductor band gap energy and is given as follows:

$$E_g(T) = E_0 - \alpha T^2/(T + \beta)$$

where $E_g(0)$ is the band gap value at 0 K and α and β are the Varshni fitting parameters characteristic of the given material. For $Li_2In_2GeSe_6$, we established $E_g(0)$ = 2.47 eV, whereas the parameters are $\alpha = 4 \times 10^{-3}$ eV/K and β = 1700 K. In Table 4, these fitting parameters are listed for germanium, gallium arsenide, $LiInSe_2$, $LiGaSe_2$, $LiGaGe_2Se_6$ (LGGSe), and $Li_2In_2GeSe_6$ (LIGSe). Parameters for the latter are rather close to those for other Li-containing chalcogenides.

Two possible variants of the E_g temperature dependence are known.[40] Some materials, such as the II−IV−V$_2$ compounds (e.g., $ZnGeAs_2$), exhibit the standard behavior when the band gap E_g monotonically decreases with increasing temperature.
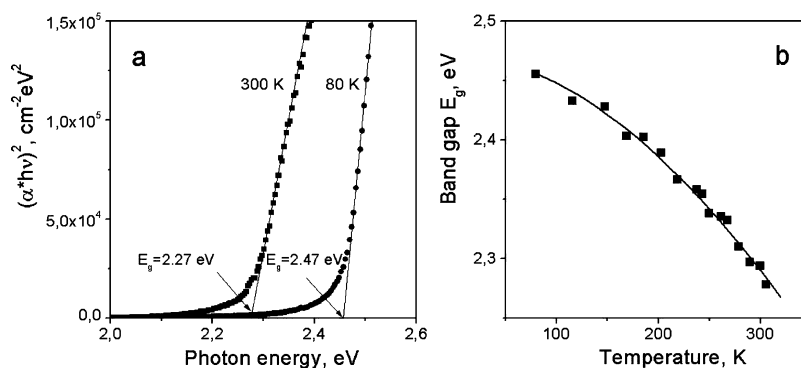

Figure 5. (a) Tauc plot for the $Li_2In_2GeSe_6$ plate about 60 μm thick. The case of direct electronic transitions. The obtained E_g values are 2.27 and 2.47 eV at 300 and 80 K, respectively. (b) Band gap vs temperature for $Li_2In_2GeSe_6$. Calculation result (line) and experimental points. Fitting: $E_g = E_0 - \alpha \times T^2/(T + \beta)$, where E_0 = 2.47 eV, $\alpha = 4 \times 10^{-3}$ eV/K, and β = 1700 K.

Table 4. Parameter Values for Modeling the Band Gap Energies

	Ge[38]	GaAs[38]	LiInSe$_2$[12]	LiGaSe$_2$[39]	LGGSe[12]	LIGSe
$E_{g(0)}$, eV	0.7437	1.519	3.07	3.68	2.64	2.47
α, eV/K	4.77×10^{-4}	5.41×10^{-4}	0.99×10^{-3}	2.28×10^{-3}	1.9×10^{-3}	4×10^{-3}
β, K	235	204	245	700	280	1700

Other compounds, such as Cu and Ag chalcopyrites, show a nonmonotonic temperature behavior with a maximum at low temperatures followed by a decrease or an extended plateau at low temperatures. Ab initio investigation showed that the nonmonotonic behavior takes place in materials with d electrons in the VB, whereas monotonic temperature dependence of the energy gap corresponds to those without d electrons (the case of Li$_2$In$_2$GeSe$_6$). The nonmonotonic behavior is explained in the model of two Bose−Einstein oscillators with weights of opposite sign leading to an increase of the band gap at low temperatures and a decrease at higher temperatures.[40]

We purposely investigated the tail of the edge of the fundamental absorption. We have not found any temperature dependence of the absorption spectrum when it is represented in ln α = $f(h\nu)$ coordinates, as in the case of the Urbach rule (the case of tails of the conduction and VBs due to disordering in the structure).[41] Thus, we assume that the dominant mechanism responsible for the slow rise of the Li$_2$In$_2$GeSe$_6$ transmission with increasing wavelength λ in the 0.65-to-1.0 μm range (Figure 4) is Rayleigh light scattering on defects: in this case, the cross section σ of the light scattering is proportional to $(1/\lambda^4)$.[41]

3.3. Raman Spectra. Raman spectra for two ternary selenides LiInSe$_2$ and LiGaSe$_2$ (panel a) and for Li$_2$In$_2$GeSe$_6$ (b) are given in Figure 6. Spectra were recorded in the backscattering geometry, in unpolarized light, at 300 K. Ternary selenides are of orthorhombic symmetry (space group $Pna2_1$), whereas Li$_2$In$_2$GeSe$_6$ is of monoclinic symmetry (Cc).
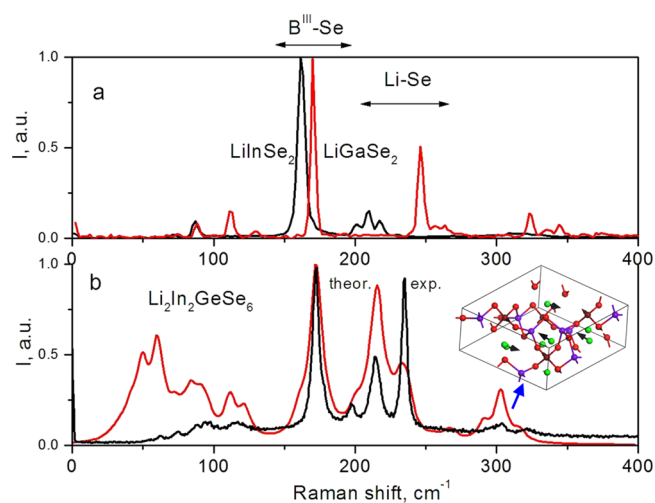

Figure 6. Raman spectra for ternary LiInSe$_2$ and LiGaSe$_2$ (a) and for Li$_2$In$_2$GeSe$_6$ quaternary chalcogenide (b). In panel (b), the black line shows an experimental spectrum, whereas the red line corresponds to a simulated one. The inset in (b) displays the vibration assignment of the mode with maximum frequency. Li, In, Ge, and Se are shown in the inset as green, violet, dark red, and red spheres, respectively.

There are three main groups of lines in all of these spectra: A (50−130 cm^{-1}, low frequencies), B (160−240 cm^{-1}, medium frequencies), and C (290−330 cm^{-1}, high frequencies). The components of these groups for experimental Li$_2$In$_2$GeSe$_6$ spectrum are listed in Table 5. Analysis of line position for

Table 5. Components in Experimental and Calculated Raman Spectra for Li$_2$In$_2$GeSe$_6$^{a}

	experimental Raman spectrum	calculated Raman spectrum
A	61.8, 74, 91, 114.6, and 125.4	**49.8**, **59.6**, 73.8, 84.7, 90.2, 112.0, 121.6
B	**172**, 197, **215**, and **234.4** cm^{-1}	**171.9**, 199.1,**206.0**, **234.0**
C	302.9 and 318.5 cm^{-1}	267.8, 291.9, **302.8**, 315.8

^{a}The most intense lines are shown bold above. The most intense lines are additionally underlined.

compounds in the LiBC$_2$ family (where B = In and Ga and C = S and Se) and line shift when replacing S with Se or In with Ga allowed the authors[42] to assign medium frequency modes in the 150−180 cm^{-1} range to B^{III}−Se vibrations, and those in the 200−280 cm^{-1} range to Li−Se vibrations. By analogy, intense lines near 172 and 234 cm^{-1} in the Raman spectrum of Li$_2$In$_2$GeSe$_6$ (Figure 6b, black line) may be related to In−Se and Ge−Se vibrations. One can notice a broad-band background in the Raman spectra of quaternary Li$_2$In$_2$GeSe$_6$ and LiGaGe$_2$Se$_6$ crystals, in contrast to the cases of ternary LiInSe$_2$ and LiGaSe$_2$. This may indicate some disorder in quaternary compounds. In the case of Li$_2$In$_2$GeSe$_6$, one of the reasons is the fact that Li atoms occupy two crystallographically nonequivalent Li1 and Li2 in the Li1Se$_4$ and Li2Se$_4$ tetrahedra, respectively.

3.4. Luminescence Spectra. The luminescence spectrum for Li$_2$In$_2$GeSe$_6$ recorded at 80 K is given in Figure 7 (curve 1). PL was excited with 0.532 μm photons: this corresponds to band-to-band excitation. The PL spectra demonstrate three broad bands at 0.837, 0.737, and 0.6356 μm (peaks 1−3, respectively). PL is rather intense at 80 K, but its intensity decreases by several orders of magnitude at room temperature. The results of deconvolution of low-temperature PL spectra into three Gaussians are given in Table 6. A narrow line at 0.5541 μm is related to the recombination of free excitons. The exciton PL line in Li$_2$In$_2$GeSe$_6$ samples means that these crystals, shown in Figure 1, are of rather high optical quality. Broad bands are associated with recombination in some point defects supposedly in native defects such as vacancies and cation antisite defects. Taking into account that ionic radii in the tetrahedral coordination are 0.59, 0.62, and 0.39 Å for Li$^+$, In^{3+}, and Ge^{4+}, respectively,[43] we suppose that possible cation antisite defects in Li$_2$In$_2$GeSe$_6$ are Ge$_{In}$ and Ge$_{Li}$ as well as Li$_{In}$ and In$_{Li}$.

Li$_2$In$_2$GeSe$_6$ crystals demonstrate unusual spontaneous emission in the 80−200 K range on heating or cooling the sample (Figure 8). This spontaneous emission is called pyroelectric luminescence (PEL) or pyroluminescence. Ten classes of pyroelectric crystals with point groups 1, 2, m, $mm2$,
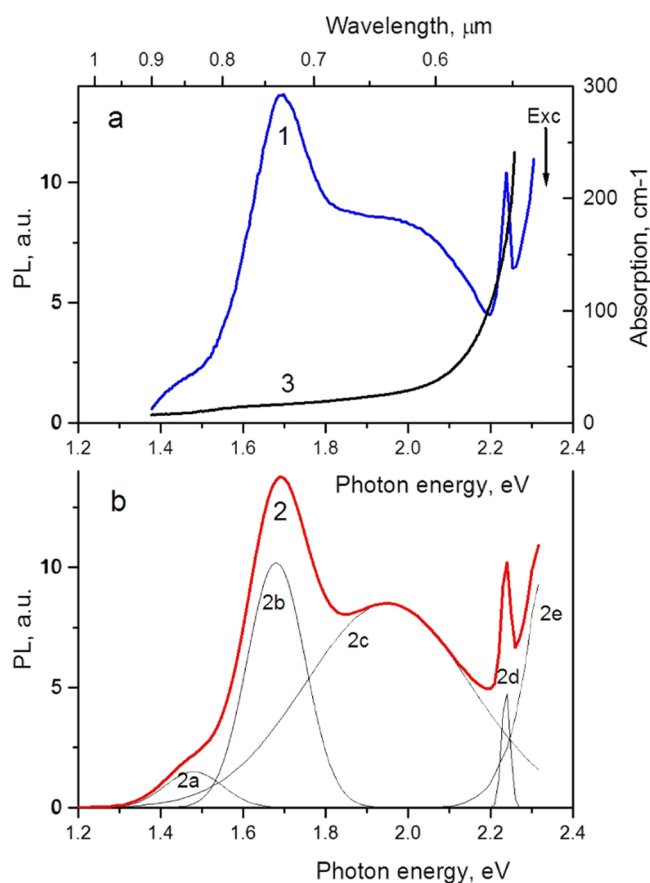
Figure 7. Experimental PL spectrum for $Li_2In_2GeSe_6$ at 0.532 μm excitation at 80 K (1) and result of its deconvolution (2) into Gaussian components (2a, 2b, 2c, and 2d). Curve (3) shows the absorption spectrum at 300 K. The exc arrow shows the photon energy of PL excitation.

Figure 8. Spontaneous emission in $Li_2In_2GeSe_6$ on heating: PEL. The sample was heated at a permanent rate of 40 K/min.

3, 3m, 4, 4mm, 6, and 6mm demonstrate such an effect. $Li_2In_2GeSe_6$ with the Cc space group and m point group is typical pyroelectric. Many of other NLO crystals are known to show such pyroluminescence: KDP, triglycine sulfate $(NH_2CH_2COOH)_3 \cdot H_2SO_4$, proustite Ag_3AsS_3 and pyrargyrite Ag_3SbS_3, beta barium borate BBO, lithium niobate $LiNbO_3$, iodate $LiIO_3$, and metagermanate Li_2GeO_3.[44] In the $LiBC_2$ family with B = In and Ga and C = S and Se with an orthorhombic structure, all members are pyroelectrics (point group $mm2$), whereas tellurides (C = Te) are not pyroelectrics: they crystallize in the chalcopyrite structure of $-42m$ symmetry.[45] All other known quaternary Li-containing chalcogenides such as $LiGa_{0.5}In_{0.5}Se_2$,[46] $Li_2Ga_2GeS_6$,[47] and $Li_2Ga_2GeSe_6$[48] are also pyroelectrics with an orthorhombic structure ($mm2$). PEL is observed commonly at low temperatures, whereas at higher temperatures, the electrical conductivity of crystals increases and PEL disappears because
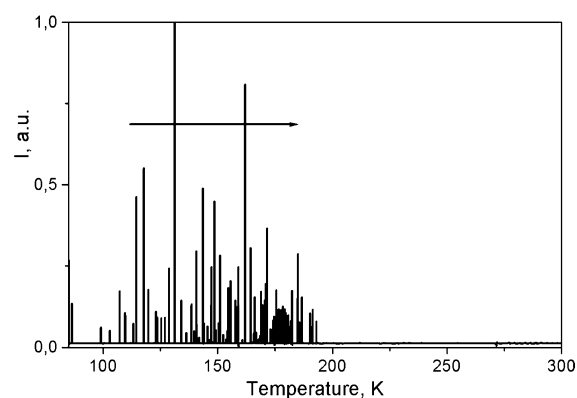
of charge leakage: in $Li_2In_2GeSe_6$, this occurs at $T > 200$ K (Figure 7a). On the other hand, the PEL intensity increases considerably in the temperature ranges at which phase transitions take place,[44] but this is not our case.

The presence of PEL must be taken into account in SHG experiments. Thus, in $Li_2In_2GeSe_6$, at excitation of about 1.06 μm, two-photon absorption enters the region of strong absorption of this crystal (Figure 4). This means that the crystal heats up strongly at the excitation point, and a strong PEL signal is observed. In this case, it is difficult to register the SHG signal because the SHG signal itself is also strongly absorbed.

3.5. Calculated Electronic and Optical Results. To elaborate the mechanism of experimentally observed optical properties of $Li_2In_2GeSe_6$, the electronic structure, phonon spectrum, refractive index dispersion, and nonlinear susceptibility are calculated by ab initio simulation based on the plane-wave pseudopotential DFT. The calculated electronic structure revealed that $Li_2In_2GeSe_6$ is a direct transition semiconductor with both the VB maximum and CB minimum located at the $\Gamma(0,0,0)$ point (Figure 9a), in good agreement with the result obtained from the transmission spectrum (section 3.2). The theoretical band gap (1.81 eV) smaller than the observed value (2.46 eV) is attributed to the discontinuity of the localized form of PBE functionals. The partial density of states (PDOS) projected onto the constituent atoms is plotted in Figure 9b, and some characteristics can be deduced:

(1) The energy levels below -10 eV are mainly composed of In 5s, Ge 4s, and Se 4s orbitals. These orbitals are difficult to be excited by the perturbation of the external photoelectric field and almost have nothing in common with the optical properties related to the electron transition across the forbidden bands. Moreover, these orbitals strongly hybridize with each other, manifesting a strong covalent interaction within $InSe_4$ and $GeSe_4$ tetrahedra.

Table 6. Parameters of PL Features in $Li_2In_2GeSe_6$ (Deconvolution Results)

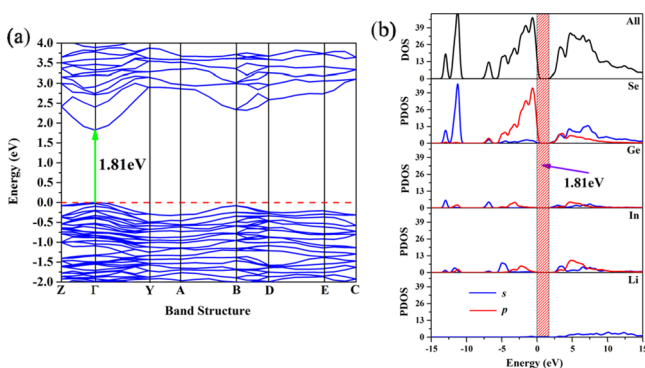| NN	description	max position E, eV	max position λ, μm	full width at half-maximum, eV	assignment
1	broad band 1	1.48	0.8375	0.17	recombination in point defects
2	broad band 2	1.68	0.7378	0.173	
3	broad band 3	1.95	0.6356	0.48	
4	narrow line	2.237	0.5541	0.024	exciton recombination

Figure 9. (a) Calculated band structure along a highly symmetric path in the Brillouin zone and (b) PDOS projected onto the constituent atoms in $Li_2In_2GeSe_6$. The band gap is highlighted by pink shadow in (b).

(2) In 5s 5p, Ge 4s 4p and Se 4s 4p orbitals construct the electron states at the top of the VB and at bottom of the CB. Moreover, the orbitals of lithium almost contribute nothing to any states, highlighting its strong ionicity. This implies that the optical properties of $Li_2In_2GeSe_6$ are predominantly determined by the electronic stimulation within $InSe_4$ and $GeSe_4$ tetrahedra.

(3) The VB is formed by (s) and (p) states in $Li_2In_2GeSe_6$ (Figure 9b). This agrees well with the monotonic temperature dependence of the band gap in $Li_2In_2GeSe_6$ (Figure 5a).[40]

The lattice vibrational behavior of $Li_2In_2GeSe_6$ is also calculated to shed light on the related experimental optical property. As shown in Figure 10, no imaginary frequency is
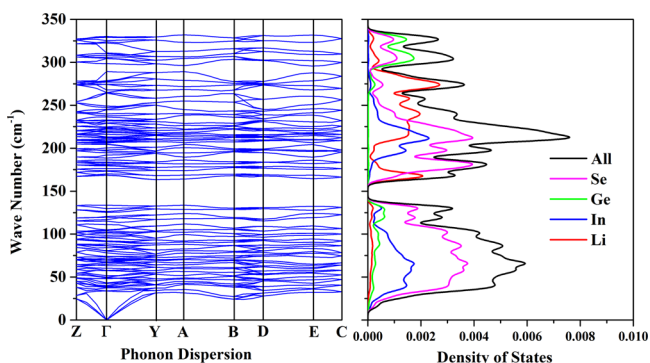

Figure 10. Phonon dispersion and density of states of $Li_2In_2GeSe_6$.

observed in the phonon spectrum, confirming the dynamical stability of the crystal structure determined by Rietveld refinement. The maximum frequency cutoff of the phonon spectrum is located at around 330 cm^{-1}, in rather good agreement with the highest frequency shift (318.5 cm^{-1}) in the measured Raman spectrum and the IR cutoff (17 μm) in the transmittance spectrum under the framework of two-phonon absorption approximation. The whole phonon spectrum is divided into two parts by a gap between 130 and 170 cm^{-1}. In both parts, the phonon branch exhibits a relatively strong dispersion, indicating the prominent coupling of the atomic vibration and manifesting the relatively strong interaction between the constituent atoms. Virtually, all constituent atoms contribute to the phonon mode in both two parts, which agree with the strong atomic interaction deduced from the phonon

dispersion. It should be emphasized that the contribution of lithium to the high-frequency part is more significant than that to the low-frequency part, especially to the maximum-frequency phonon mode. Moreover, the Raman spectrum was also simulated, and clearly good agreement is achieved between the calculated and measured results (Figure 8b). According to the simulated vibration assignment, the maximum-frequency phonon modes (318 and 325 cm^{-1} in the measured and simulated spectra) are mainly ascribed to the translation vibration of lithium ions (the inset in Figure 8b). This indicates that the light lithium element plays a key role in determining the mid-IR absorption edge.

The first-principles calculations gave the following values of second-order nonlinear susceptibility of $Li_2In_2GeSe_6$: $d_{11} = -8.3$ pm/V; $d_{15} = 6.1$ pm/V; $d_{12} = 2.0$ pm/V; $d_{13} = 7.2$ pm/V; $d_{24} = -5.8$ pm/V; and $d_{33} = 1.7$ pm/V. One can see that these values are close to those for ternary Li-containing chalcogenides: $d_{31} = 7.2$ pm/V, $d_{32} = 5.7$ pm/V for $LiInS_2$ and $d_{31} = 10.4$ pm/V, and $d_{32} = 7.8$ pm/V for $LiInSe_2$.[1] These values are several times ($\sim$3.5) lower than the second-order nonlinear susceptibility for $AgGaSe_2$ single crystal d_{36} (at 9.2714 μm) = 39 pm/V.[1] Thus, nonlinear susceptibility for $AgGaSe_2$ is about 3 times larger than that for $Li_2In_2GeSe_6$. This differs from the results in ref 14, where SHG signals were found to be close to each other for powders of $Li_2In_2GeSe_6$ and $AgGaSe_2$. A probable reason of such contradiction is that SHG signals were measured on powders in ref 14, whereas the above given values for $Li_2In_2GeSe_6$ and $AgGaSe_2$ are related to bulk single crystals. It is necessary to take into account that SHG signals depend considerably on the grain size in the powder and this behavior varies considerably for different compounds. For example, the SHG signal grows by several times monotonically in $AgGaS_2$ and $PbGa_2GeSe_6$ when the grain size increases from 30 to 200 μm.[49] On the other hand, $Ba_{23}Ga_8Sb_{23}S_{38}$ demonstrates an opposite behavior: the SHG signal decreases by an order of magnitude as the grain size increases in the same size range.[50] Thus, it is necessary to estimate nonlinear susceptibilities for bulk $Li_2In_2GeSe_6$ crystals, and this work is in progress.

Additionally, the calculated dispersive refractive index revealed that the birefringence (Δn) of $Li_2In_2GeSe_6$ is as high as 0.043 near 1.064 μm (Figure 11), which exceeds the value of $AgGaSe_2$ ($\Delta n \approx 0.02$) by two times[1] and indicates its strong phase-matching ability.
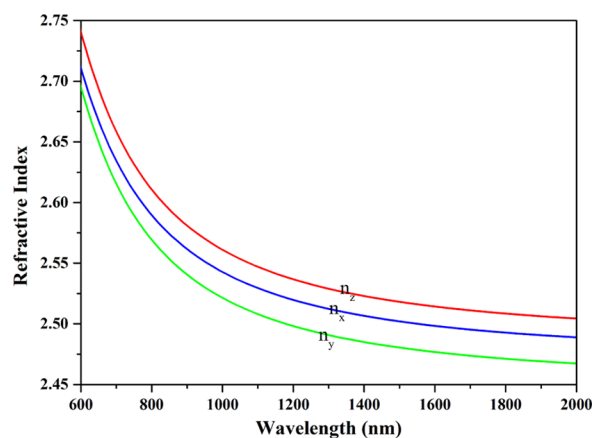

Figure 11. Calculated dispersion of the refractive indices n_x, n_y, and n_z of $Li_2In_2GeSe_6$.

4. CONCLUSIONS

Large single $Li_2In_2GeSe_6$ crystals of optical quality were grown by the Bridgman−Stockbarger technique, and the crystal structure was established. The thermal expansion parameters for $Li_2In_2GeSe_6$ were determined: their increase on heating was found to be monotonic in contrast to commercial $AgGaS_2$ and $AgGaSe_2$. The transparency range is 0.55−17 μm with a strong absorption of water, Ge−O, and Se−Se complexes: water absorption can be removed by repolishing or annealing. Tauc analysis showed direct band-to-band electronic transitions and band gap values of E_g = 2.27 and 2.47 eV at 300 and 80 K, respectively. The Raman spectrum demonstrates vibrations within the 350 cm^{-1} range with the main modes at 172, 215, and 234.4 cm^{-1}: the two-phonon absorption determines the long-wavelength edge of the transparency range near 17 μm.

Three broad bands near 0.837, 0.737, and 0.6356 μm are supposedly associated with cation antisite defects in the luminescence spectra. A narrow line at 0.554 μm corresponds to exciton recombination, and this confirms the high quality of grown $Li_2In_2GeSe_6$ crystals.

Electronic structure, density of states, and some optical properties were calculated from the first principles for $Li_2In_2GeSe_6$. Nonlinear coefficients are within 8.3 pm/V; a birefringence of 0.043 at 1.064 μm indicates the strong phase-matching ability. On the basis of our systematic investigations, we believe that $Li_2In_2GeSe_6$ is a promising NLO crystal that can be used in the mid-IR region.

ASSOCIATED CONTENT

Ⓢ Supporting Information

The Supporting Information is available free of charge on the ACS Publications website at DOI: 10.1021/acs.jpcc.8b02799.

> Fractional atomic coordinates and isotropic displacement parameters, main bond lengths, and X-ray powder patterns in the temperature range of 303−723 K (PDF)
> X-ray crystallographic data of $Li_2In_2GeSe_6$ (CIF)

AUTHOR INFORMATION

Corresponding Authors
*E-mail: eliseev.ap@mail.ru, eliseev@igm.nsc.ru (A.P.Y.).
*E-mail: zslin@mail.ipc.ac.cn (Z.L.).

ORCID Ⓘ
M. S. Molokeev: 0000-0002-8297-0945
Xingxing Jiang: 0000-0001-6068-8773
Zheshuai Lin: 0000-0002-9829-9893

Notes
The authors declare no competing financial interest.

ACKNOWLEDGMENTS

REFERENCES

(1) Nikogosyan, D. N. *Nonlinear Optical Crystals: A Complete Survey*; Springer Science Business Media, Inc.: New York, 2005.

(2) Schunemann, P. G. Crystal Growth and Nonlinear Materials. *AIP Conf. Proc.* **2007**, *916*, 541−559.

(3) Fossier, S.; Salaün, S.; Mangin, J.; Bidault, O.; Thénot, I.; Zondy, J.-J.; Chen, W.; Rotermund, F.; Petrov, V.; Petrov, P.; et al. Optical, vibrational, thermal, electrical, damage, and phase-matching properties of lithium thioindate. *J. Opt. Soc. Am. B* **2004**, *21*, 1981−2007.

(4) Petrov, V.; Zondy, J.-J.; Bidault, O.; Isaenko, L.; Vedenyapin, V.; Yelisseyev, A.; Chen, W.; Tyazhev, A.; Lobanov, S.; Marchev, G.; et al. Optical, thermal, electrical, damage, and phase-matching properties of lithium selenoindate. *J. Opt. Soc. Am. B* **2010**, *27*, 1902−1927.

(5) Isaenko, L.; Yelisseyev, A.; Lobanov, S.; Krinitsin, P.; Petrov, V.; Zondy, J.-J. Ternary chalcogenides LiBC2 (B=In,Ga; C=S,Se,Te) for mid-IR nonlinear optics. *J. Non-Cryst. Solids* **2006**, *352*, 2439−2443.

(6) Badikov, V. V.; Tyulyupa, A. G.; Sheverdyaeva, G. S.; Sheina, S. G. Solid Solutions in the $AgGaS_2$-GeS_2 and $AgGaSe_2$-$GeSe_2$ Systems. *Inorg. Mater.* **1991**, *27*, 177−185.

(7) Petrov, V.; Badikov, V.; Shevyrdyaeva, G.; Panyutin, V.; Chizhikov, V. Phase-matching properties and optical parametric amplification in single crystals of AgGaGeS4. *Opt. Mater.* **2004**, *26*, 217−222.

(8) Schunemann, P. G. Growth of New Quaternary Nonlinear Optical Crystals for 1-micron-Pumped Mid-IR Generation. *Proc. SPIE* **2006**, *6103*, 610303.

(9) Kim, Y.; Seo, I.-s.; Martin, S. W.; Baek, J.; Halasyamani, P. S.; Arumugam, N.; Steinfink, H. Characterization of New Infrared Nonlinear Optical Material with High Laser Damage Threshold, Li2Ga2GeS6. *Chem. Mater.* **2008**, *20*, 6048−6052.

(10) Mei, D.; Yin, W.; Feng, K.; Lin, Z.; Bai, L.; Yao, J.; Wu, Y. LiGaGe2Se6: A New IR Nonlinear Optical Material with Low Melting Point. *Inorg. Chem.* **2012**, *51*, 1035−1040.

(11) Lavrentyev, A. A.; Gabrelian, B. V.; Vu, V. T.; Ananchenko, L. N.; Isaenko, L. I.; Yelisseyev, A.; Krinitsin, P. G.; Khyzhun, O. Y. Electronic structure and optical properties of noncentrosymmetric LiGaGe 2 Se 6, a promising nonlinear optical material. *Phys. B* **2016**, *501*, 74−83.

(12) Yelisseyev, A. P.; Isaenko, L. I.; Krinitsin, P.; Liang, F.; Goloshumova, A. A.; Naumov, D. Y.; Lin, Z. Crystal Growth, Structure, and Optical Properties of LiGaGe2Se6. *Inorg. Chem.* **2016**, *55*, 8672−8680.

(13) Isaenko, L.; Vasilyeva, I.; Merkulov, A.; Yelisseyev, A.; Lobanov, S. Growth of new nonlinear crystals LiMX2 (M=Al, In, Ga; X=S, Se, Te) for the mid-IR optics. *J. Cryst. Growth* **2005**, *275*, 217−223.

(14) Yin, W.; Feng, K.; Hao, W.; Yao, J.; Wu, Y. Synthesis, Structure, and Properties of Li2In2MQ6 (M = Si, Ge; Q = S, Se): A New Series of IR Nonlinear Optical Materials. *Inorg. Chem.* **2012**, *51*, 5839−5843.

(15) Stove, A. C.; Morrell, J.; Battacharya, P.; Tupitsyn, E.; Burger, A. Synthesis of a Potential Semiconductor neutron Detector Crystal LiGa(Se/Te)₂: Materials Purity and Compatibility Effects. *Proc. SPIE* **2011**, *8142*, 81421H.

(16) Tupitsyn, E.; Bhattacharya, P.; Rowe, E.; Matei, L.; Cui, Y.; Buliga, V.; Groza, M.; Wiggins, B.; Burger, A.; Stowe, A. Lithium Containing Chalcogenide Single Crystals for Neutron Detection. *J. Cryst. Growth* **2014**, *393*, 23−27.

(17) Tauc, J. Optical Properties and Electronic Structure of Amorphous Ge and Si. *Mater. Res. Bull.* **1968**, *3*, 37−46.

(18) Kohn, W.; Sham, L. J. Self-Consistent Equations Including Exchange and Correlation Effects. *Phys. Rev. [Sect.] A* **1965**, *140*, A1133.

(19) Payne, M. C.; Teter, M. P.; Allan, D. C.; Arias, T. A.; Joannopoulos, J. D. Iterative minimization techniques forab initiototal-energy calculations: molecular dynamics and conjugate gradients. *Rev. Mod. Phys.* **1992**, *64*, 1045−1097.

(20) Clark, S. J.; Segall, M. D.; Pickard, C. J.; Hasnip, P. J.; Probert, M. I. J.; Refson, K.; Payne, M. C. First Principles Methods using CASTEP. *Z. Kristallogr.* **2005**, *220*, 567−570.

(21) Perdew, J. P.; Burke, K.; Ernzerhof, M. Generalized Gradient Approximation Made Simple. *Phys. Rev. Lett.* **1996**, *77*, 3865−3868.

(22) Hamann, D. R.; Schlüter, M.; Chiang, C. Norm-Conserving Pseudopotentials. *Phys. Rev. Lett.* **1979**, *43*, 1494−1497.

(23) Monkhorst, H. J.; Pack, J. D. Special Points for Brillouin-Zone Integrations. *Phys. Rev. B: Solid State* **1976**, *13*, 5188−5192.

(24) Godby, R. W.; Schlüter, M.; Sham, L. J. Self-Energy Operators and Exchange-Correlation Potentials in Semiconductors. *Phys. Rev. B: Condens. Matter Mater. Phys.* **1988**, *37*, 10159−10175.

(25) Lin, Z.; Jiang, X.; Kang, L.; Gong, P.; Luo, S.; Lee, M.-H. First-Principles Materials Applications and Design of Nonlinear Optical Crystals. *J. Phys. D: Appl. Phys.* **2014**, *47*, 253001.

(26) Lin, J.; Lee, M.-H.; Liu, Z.-P.; Chen, C.; Pickard, C. J. Mechanism for linear and nonlinear optical effects inβ−BaB2O4c-rystals. *Phys. Rev. B: Condens. Matter Mater. Phys.* **1999**, *60*, 13380−13389.

(27) Palik, E. D. *Handbook of Optical Constants of Solids*; Academic: New York, 1985.

(28) Baroni, S.; de Gironcoli, S.; Dal Corso, A.; Giannozzi, P. Phonons and Related Crystal Properties from Density-Functional Perturbation Theory. *Rev. Mod. Phys.* **2001**, *73*, 515−562.

(29) Deyirmenjian, V. B.; Heine, V.; Payne, M. C.; Milman, V.; Lynden-Bell, R. M.; Finnis, M. W. Ab initioatomistic simulation of the strength of defective aluminum and tests of empirical force models. *Phys. Rev. B: Condens. Matter Mater. Phys.* **1995**, *52*, 15191−15207.

(30) *Bruker AXS TOPAS V4: General Profile and Structure Analysis Software for Powder Diffraction Data. User's Manual*; Bruker AXS: Karlsruhe, Germany, 2008.

(31) Beister, H. J.; Ves, S.; Hönle, W.; Syassen, K.; Kühn, G. Structural phase transitions and optical absorption ofLiInSe2under pressure. *Phys. Rev. B: Condens. Matter Mater. Phys.* **1991**, *43*, 9635−9642.

(32) Iseler, G. W. Thermal expansion and seeded bridgman growth of AgGaSe2. *J. Cryst. Growth* **1977**, *41*, 146−150.

(33) Yelisseyev, A. P.; Drebushchak, V. A.; Titov, A. S.; Isaenko, L. I.; Lobanov, S. I.; Lyapunov, K. M.; Gruzdev, V. A.; Komarov, S. G.; Petrov, V.; Zondy, J.-J. Thermal properties of the midinfrared nonlinear crystal LiInSe2. *J. Appl. Phys.* **2004**, *96*, 3659−3665.

(34) Kokorina, V. F. *Glasses for Infrared Optics*; CRC Press, 1996.

(35) Aarik, J.; Mändar, H.; Kirm, M.; Pung, L. Optical characterization of HfO2 thin films grown by atomic layer deposition. *Thin Solid Films* **2004**, *466*, 41−47.

(36) Varshni, Y. P. Temperature Dependence of the Energy Gap in Semiconductors. *Physica* **1967**, *34*, 149−154.

(37) O'Donnel, K. P.; Chen, X. Temperature Dependence of Semiconductor Band Gaps. *Appl. Phys. Lett.* **1991**, *58*, 2924−2926.

(38) Sze, S. *Physics of Semiconductor Devices*, 2nd ed.; Wiley: New York, 1981.

(39) Yelisseyev, A.; Liang, F.; Isaenko, L.; Lobanov, S.; Goloshumova, A.; Lin, Z. S. Optical properties of LiGaSe 2 noncentrosymmetric crystal. *Opt. Mater.* **2017**, *72*, 795−804.

(40) Bhosale, J.; Ramdas, A. K.; Burger, A.; Muñoz, A.; Romero, A. H.; Cardona, M.; Lauck, R.; Kremer, R. K. Temperature Dependence of Band Gaps in Semiconductors: Electron-phonon interaction. *Phys. Rev. B: Condens. Matter Mater. Phys.* **2012**, *86*, 195208.

(41) Studenyak, I.; Kranjčec, M.; Kurik, M. Urbach Rule in Solid State Physics. *Int. J. Optic. Appl.* **2014**, *4*, 94−104.

(42) Eifler, A.; Riede, V.; Brückner, J.; Weise, S.; Krämer, V.; Lippold, G.; Schmitz, W.; Bente, K.; Grill, W. Band Gap Energies and Lattice Vibrations of the Lithium Ternary Compounds LiInSe2, LiInS2, LiGaSe2and LiGaS2. *Jpn. J. Appl. Phys.* **2000**, *39*, 279−283.

(43) Shannon, R. D. Revised effective ionic radii and systematic studies of interatomic distances in halides and chalcogenides. *Acta Cryst Sect A* **1976**, *32*, 751−767.

(44) Yelisseyev, A. P.; Isaenko, L. I.; Starikova, M. K. Optical study of defects in lithium iodate α-LiIO_3. *J. Opt. Soc. Am. B* **2012**, *29*, 1430−1435.

(45) Yelisseyev, A.; Krinitsin, P.; Isaenko, L.; Grazhdannikov, S. Spectroscopic properties of nonlinear optical LiGaTe2 crystal. *Opt. Mater.* **2015**, *42*, 276−280.

(46) Isaenko, L.; Yelisseyev, A.; Lobanov, S.; Vedenyapin, V.; Krinitsyn, P.; Petrov, V. Properties of LiGa0.5In0.5Se2: A Quaternary Chalcogenide Crystal for Nonlinear Optical Applications in the Mid-IR. *Crystals* **2016**, *6*, 85−96.

(47) Isaenko, L. I.; Yelisseyev, A. P.; Lobanov, S. I.; Krinitsin, P. G.; Molokeev, M. S. Structure and optical properties of Li2Ga2GeS6 nonlinear crystal. *Opt. Mater.* **2015**, *47*, 413−419.

(48) Yelisseyev, A. P.; Isaenko, L. I.; Krinitsin, P.; Liang, F.; Goloshumova, A. A.; Naumov, D. Y.; Lin, Z. Crystal Growth, Structure, and Optical Properties of LiGaGe2Se6. *Inorg. Chem.* **2016**, *55*, 8672−8680.

(49) Luo, Z.-Z.; Lin, C.-S.; Cui, H.-H.; Zhang, W.-L.; Zhang, H.; Chen, H.; He, Z.-Z.; Cheng, W.-D. PbGa2MSe6 (M = Si, Ge): Two Exceptional Infrared Nonlinear Optical Crystals. *Chem. Mater.* **2015**, *27*, 914−922.

(50) Chen, M.-C.; Wu, L.-M.; Lin, H.; Zhou, L.-J.; Chen, L. Disconnection Enhances the Second Harmonic Generation Response: Synthesis and Characterization of Ba23Ga8Sb2S38. *J. Am. Chem. Soc.* **2012**, *134*, 6058−6060.